Supplementary Information for

Low-coordinated Co-Mn diatomic sites derived from metal-organic framework nanorod promote electrocatalytic CO_2 reduction

Jiajing Pei,‡[a,b] Guikai Zhang,‡[a,c] Jiangwen Liao,[a,c] Shufang Ji,[d] Huan Huang,[a] Ping Wang,[b] Pengfei An,*[a] Shengqi Chu*[a] and Juncai Dong*[a,c]

Table of contents

Reagents. Cobalt (II) acetate, nickel Manganese acetate, Zinc nitrate hexahydrate ($Zn(NO_3)_2 \cdot 6H_2O$), 2-methylimidazole, cetyltrimethylammonium bromide (CTAB), tetraethyl orthosilicate, Potassium bicarbonate ($KHCO_3$, 99.999%), Nafion D-521 dispersion (5% w/w in water and 1-propanol), were purchased from Alfa Aesar. Methanol, ethanol and sodium hydroxide (analytical grade) were obtained from Sinopharm Chemical. Nafion 211 membrane was purchased from Dupont. 18.2 MΩ cm ultrapure water was purified by milli-Q instrument. High purity Helium gas (99.9999%) and carbon dioxide (99.999%) were purchased at Haipu Gas Company. All the chemicals were analytical grade and used without further purification.

Synthesis of L-Co_1Mn_1-NC DS catalyst. Briefly, a solution was prepared by dissolving 1.813 g of $Zn(NO_3)_2 \cdot 6H_2O$ and 17.5 mg of CTAB in 12.5 ml of H_2O, while 5.6752 g of 2-methylimidazole was dissolved in 87.5 ml of H_2O. The two solutions were combined and agitated for a duration of 5 minutes, after which they were allowed to stand at room temperature for a period of 3 hours. After that, the white ZIF-8 nanorod precipitate was subjected to centrifugation, followed by multiple washes with methanol and H_2O, and then dried at 60 °C under vacuum conditions. Subsequently, 300 mg of ZIF-8 nanorods were dispersed using ultrasonication in a solution consisting of 100 ml of ultrapure water. To this dispersion, 75 mg CTAB and 30 mg NaOH were introduced and stirred for a duration of 5 minutes. a solution comprising 0.6 mL of tetraethyl orthosilicate in 3 mL of methanol was incrementally introduced into the mixture with continuous stirring. After being stirred for a duration of 30 minutes, the resultant solution underwent centrifugation, washing, and subsequent vacuum drying at a temperature of 60 °C over the course of the night. The ZIF-8@SiO_2 powder was subsequently subjected to pyrolysis at a temperature of 650 °C for a duration of 2 h in an argon atmosphere within a tube furnace. The resultant products were subsequently distributed in a 3 M NaOH solution and agitated at a temperature of 50 °C for a duration of 12 h. Following this, the combination was subjected to centrifugation, rinsed with ultrapure water to achieve a neutral pH, and dried at a temperature of 60 °C in order to acquire the nanorod-shaped substrate. 200 mg of carbon carrier was accurately weighed

and then dispersed in 50 mL of ethanol. The dispersion was then subjected to sonication for a duration of 1 hour to ensure a homogeneous distribution. Subsequently, 0.6 mL of $Co(oAc)_2$ and 0.4 mL of $Mn(oAc)_2$ ethanol solution (10 mg/mL) were added dropwised in turn, followed by stirring for 24 h. The resulting mixture was then stirred for a duration of 24 hours, after which the mixtures were subjected to drying at 60 °C under vacuum conditions. The L-Co_1Mn_1-NC DS catalyst was synthesized through the calcination of the powder at a temperature of 1000 °C for a duration of 2 h in an Ar atmosphere.

Synthesis of Co_1Mn_1-NC DS catalyst. The synthesis procedures of Co_1Mn_1-NC were similar to that of L-Co_1Mn_1-NC sample, except that the finally pyrolysis temperature was changed to 900 °C for 3 h.

Synthesis of Co_1-NC and Mn_1-NC catalyst. The synthesis procedures of individual Co_1-NC and Mn_1-NC catalysts were similar to that of L-Co_1Mn_1-NC sample, except that the finally pyrolysis temperature was changed to 900 °C for 3 h and only one metal precursor (Co or Mn) was added at the same time.

Characterizations. The configuration of the atomic catalysts was examined using transmission electron microscopy (TEM) recorded by H7700 instrument, and scanning electron microscopy (SEM) images were captured with the Hitachi-SU8010 instrument. Images for EDS mapping were obtained utilizing a JEM-2010F electron microscope fitted with an energy-dispersive X-ray spectrometer, functioning at 200 kV. The HAADF-STEM images were captured using a JEOL JEM-ARM200F microscope with an acceleration voltage of 300 kV. The atomic configuration of the L-Co_1Mn_1-NC catalyst was analyzed utilizing a JEOL ARM-200CF transmission electron microscope running at 200 keV and outfitted with dual spherical aberration (Cs) correctors. X-ray diffraction (XRD) patterns were obtained using a Bruker AXS D8 FOCUS X-ray powder diffractometer equipped with Cu Kα radiation. X-ray photoelectron spectroscopy (XPS) analyses were carried out utilizing a Perkin Elmer Physics PHI 5300 spectrometer with Al Kα nonmonochromatic radiation. The metal content was determined via inductively coupled plasma optical emission spectrometry (ICP-OES)

on a Thermo Fisher IRIS Intrepid II instrument. Raman spectra were collected employing a Renishaw in Via-Reflex spectrometer system excited by a 514-nm laser.

Electrochemical measurements. The electrochemical performance was evaluated by Chenhua CHI 760E with a typical three-electrode setup. A Nafion 211 membrane was placed between the cathodic and anodic chambers. Pt plate was used as the counter electrode, Ag/AgCl (saturated KCl solution) was used as the reference electrode, and the electrolyte was CO_2 saturated 0.5 M $KHCO_3$ solution. The flow rate of CO_2 was controlled at 20 sccm. Prior to the electrochemical tests, the electrolytes were further saturated with high-purity CO_2 (99.999%) for 30 minutes to eliminate dissolved oxygen. For the preparation of the working electrode, 5 mg of catalysts were mixed in a solution containing 500 μL of distilled water, 500 μL of isopropanol, and 20 μL of 5 wt% Nafion, followed by sonication for 2 h. Subsequently, 80 μL of the resulting ink was deposited onto Carbon fiber paper, achieving a mass loading of approximately 0.4 $mg \cdot cm^{-2}$. Linear sweep voltammetry measurements were conducted with a scan rate of 10 mV s^{-1}. All LSV and constant potential data are corrected by iR compensation. The iR compensation of electrochemical data was obtained mainly through the test impedance spectrum, and it was determined by potentiostatic electrochemical impedance spectroscopy at frequencies ranging from 0.1 Hz to 100 kHz. According to the Nernst equation ($E_{RHE}=E_{SCE}+0.059\times pH+0.197$ V, at 25 °C), all potentials were calculated with respect to the reversible hydrogen electrode (RHE) scale. The gas products of electrolysis were detected on the Shimazu 2014 plus gas chromatography equipped with FID detector and ShinCarbon ST 100/120 packed column.

In order to achieve a greater current density, the electrolysis configuration was modified from an H-cell to a home-made CO_2 flow cell, incorporating gas diffusion electrodes (GDL) and employing a standard three-electrode measurement setup (Fig. R10). The cathode working electrode utilized in the flow cell was the L-Co_1Mn_1-NC catalyst applied onto a GDL with a loading density of 0.6 mg cm^{-2}. The anode counter electrode employed was the IrO_2 catalyst also sprayed on a GDL with a loading of 0.6 mg cm^{-2}, occurring the oxygen evolution reaction. A Nafion 117 membrane was placed

between the cathodic and anodic chambers of flow cell. On the cathode side, electrolyte (0.5 M $KHCO_3$) was pumped by a syringe pump (PHD 2000, Harvard Apparatus) with a constant flow rate of 10 sccm. High purity CO_2 gas flowed at a rate of 50 sccm behind the cathode GDL controlled by a mass flow controller (CS200, Beijing Sevenstar). An Ag/AgCl (saturated KCl) reference electrode was employed. The solution resistance was determined by potentiostatic electrochemical impedance spectroscopy at frequencies ranging from 0.1 Hz to 100 kHz. All the measured potentials using three-electrode setup were manually compensated.

Data analysis.

According to the definition of FE:

$$FE = \frac{\alpha \times F \times n}{Q} = \frac{\alpha \times F \times n}{I_{total} \times t}$$

$$P \times V = n \times R \times T \rightarrow n = \frac{P_0 \times V_{total} \times \nu}{R \times T_0}$$

$$FE = \frac{\alpha \times F}{I_{total}} \times \frac{P_0 \times \nu}{R \times T_0} \times \frac{V_{volume}}{t} = \frac{\alpha \times F \times P_0 \times \nu \times V_{flow\,rate}}{R \times T_0 \times I_{total}}$$

Where α is the number of electrons transferred during reaction (α=2); F: Faradaic constant (96500 C mol^{-1}); P_0 is atmospheric pressure (101325 N m^{-2}); ν is gas concentration; $V_{flow\,rate}$ is volumetric flow rate; R is ideal gas constant (8.314 N m mol^{-1} K^{-1}); T_0 is reaction temperature (298,15 K); I_{total} is total current.

TOF for CO production was calculated as follow equation:

$$TOF = \frac{I_{product}/nF}{m_{cat} \times \omega / M_{metal}} \times 3600$$

TOF = turnover frequency, h^{-1}.

$I_{product}$ = partial current for certain product, A.

n = 2, the number of electrons transferred for CO production.

F = 96485 C mol^{-1}, Faradaic constant.

m_{cat} = the mass of catalyst on the carbon paper, g.

ω = metal loading in the catalyst.

M_{metal} = atomic mass of Co (58.9 g mol^{-1}) for Co_1-NC, atomic mass of Mn (54.9 g mol^{-1}) for Mn_1-NC, and atomic mass of 57.3 g mol^{-1} for diatomic site catalysts (based on the ratio of Co and Mn).

XAFS Data Analysis. The EXAFS data were processed according to the standard procedures using the Athena and Artemis implemented in the IFEFFIT software packages. The acquired EXAFS data were processed according to the standard procedures using the ATHENA module. The EXAFS spectra were obtained by subtracting the post-edge background from the overall absorption and then normalizing with respect to the edge-jump step. Subsequently, the $\chi(k)$ data were Fourier transformed to real (R) space using a hanning windows (dk=1.0 $Å^{-1}$) to separate the EXAFS contributions from different coordination shells. To obtain the quantitative structural parameters around the atoms being investigated, least-squares parameter fitting was performed using the ARTEMIS module of IFEFFIT software packages.

The following EXAFS equation was employed:

$$\chi(k)=\sum_j \frac{N_j S_o^2 F_j(k)}{k R_j^2}\exp[-2k^2\sigma_j^2]\exp[\frac{-2R_j}{\lambda(k)}]\sin[2kR_j+\phi_j(k)]$$

S_0^2 is the amplitude reduction factor, $F_j(k)$ is the effective curved-wave backscattering amplitude, N_j is the number of neighbors in the j^{th} atomic shell, R_j is the distance between the X-ray absorbing central atom and the atoms in the j^{th} atomic shell (backscatterer), λ is the mean free path in Å, $\phi_j(k)$ is the phase shift (including the phase shift for each shell and the total central atom phase shift), σ_j is the Debye-Waller parameter of the j^{th} atomic shell (variation of distances around the average R_j). The functions $F_j(k)$, λ and $\phi_j(k)$ were calculated with the ab initio code FEFF8.2. The coordination numbers of model samples were fixed as the nominal values. The obtained

S_0^2 was fixed in the subsequent fitting. While the internal atomic distances R, Debye-Waller factor σ^2, and the edge-energy shift ΔE_0 were allowed to run freely.

In situ ATR-SEIRAS Measurements. The in situ ATR-SEIRAS spectra were acquired using a Nicolet iS50 Fourier-transform infrared (FT-IR) spectrometer, which was outfitted with a mercury cadmium telluride (MCT) detector cooled by liquid nitrogen. Additionally, a PIKE VeeMAX III variable angle attenuated total reflection (ATR) sampling accessory was employed during the measurements. The resolution of IR spectra was set to 8 cm^{-1} and 64 interferograms were co-added for each spectrum. The absorption units of spectra are defined as A = −log(R/R0), where R and R0 express as the reflected IR intensity concerning the sample and reference-single beam spectrum, respectively. A crystal with a Si face angle of 60° was employed as the reflection accessory, with the incident angle being ca. 70°. A chemical deposition process is utilized to apply a thin layer of Au film onto the surface of a Si crystal in order to amplify the IR signal and facilitate the movement of electrons. Initially, we conducted in situ ATR-SEIRAS on the Au film to mitigate its impact on the signal of the CO_2RR. The catalyst ink was applied onto the Au film acting as the working electrode at a loading of 0.1 mg cm^{-2}. The ink was spread evenly over the surface of the Au film to minimize the impact of the film itself. A platinum wire was utilized as the counter electrode, while a SCE served as the reference electrode. The electrolyte employed in the experiment was a solution of 0.5 M $KHCO_3$ saturated with CO_2. During the in situ experiment, the chronopotentiometry technique was utilized to apply various potentials ranging from 0 to −1 V versus RHE without iR correction. Synchronously, ATR-SEIRAS spectra were acquired for each potential test. A reference background ATR-SEIRAS spectrum was obtained at 0 V.

Computational details. Vienna ab initio simulation package (VASP) software was used to conducted density functional theory (DFT) simulations.[1] In the calculation, generalized gradient approximation (GGA) with the Perdew-Burke-Ernzerhof (PBE) function was used to describe exchange correlation energy.[2] The projector augmented-wave (PAW) method was used to approximate the core electron states,[3] and the cutoff

energy with plane-wave basis sets was set as 450 eV. The gamma-centered k-mash of 3 × 3 × 1 and energy convergence criterion of 10^{-6} eV was used in the self-consistent calculation. The structure was relaxed until residual force was converged to 0.02 eV/Å in geometric structure optimization. Graphene-supported N-coordination metal catalysts were modeled to simulate their electronic properties and catalytic properties. The vacuum layer height was set at 15 Å to avoid interactions.

In CO_2RR reaction pathway, Gibbs free energies were calculated using

$$\Delta G = \Delta E + \Delta ZPE - \Delta TS$$

in which ΔE, ΔZPE, T and S denote the binding energy, zero-point energy, reaction temperature and entropy, respectively. The rate-determining step is defined as the reaction step with the greatest energy barrier.

Supporting Figures and Tables

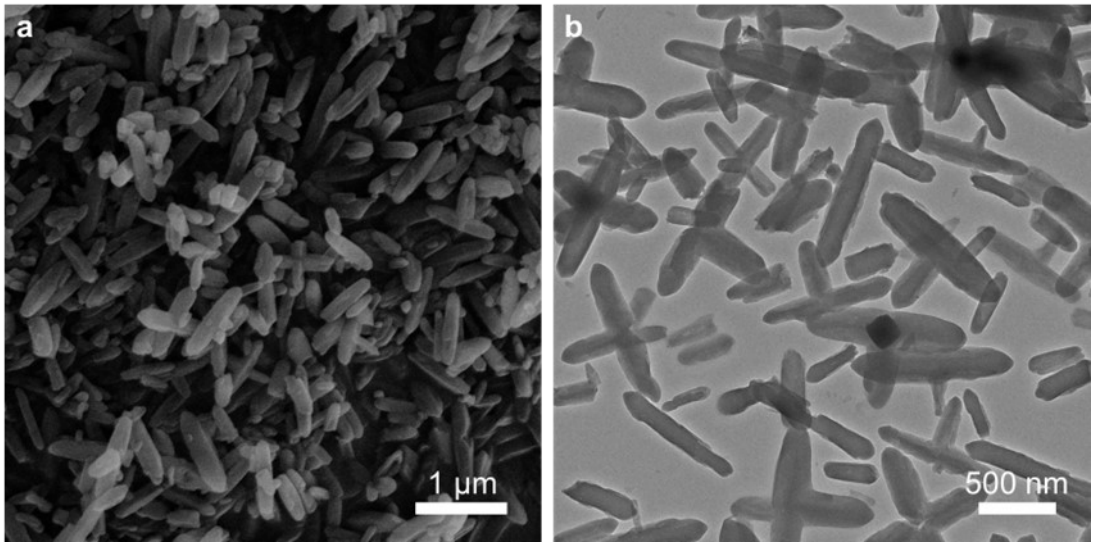

Fig. S1 The SEM (a) and TEM (b) images of ZIF-8 nanorods.

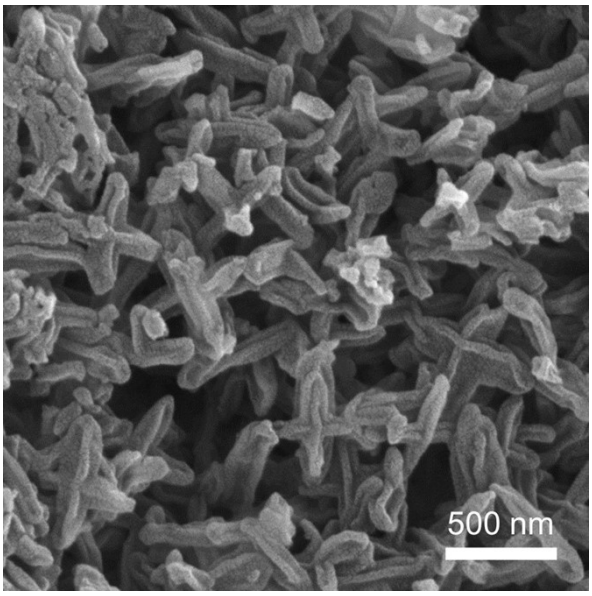

Fig. S2 The SEM image of L-Co_1Mn_1-NC catalyst.

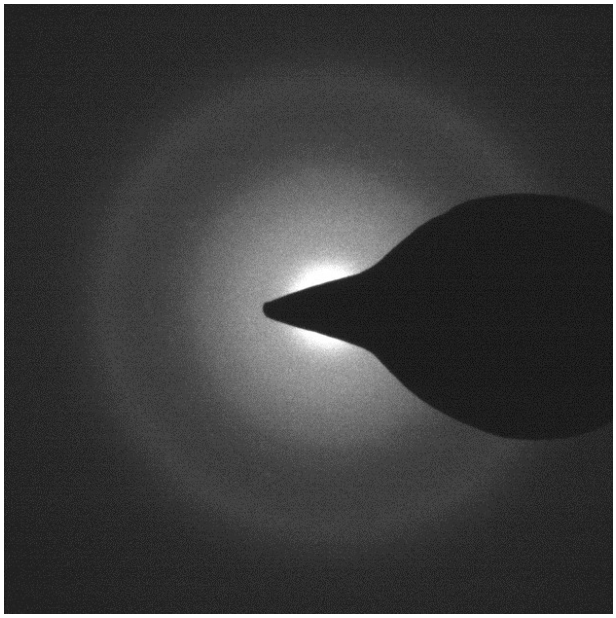

Fig. S3 The SEAD image of L-Co_1Mn_1-NC catalyst.

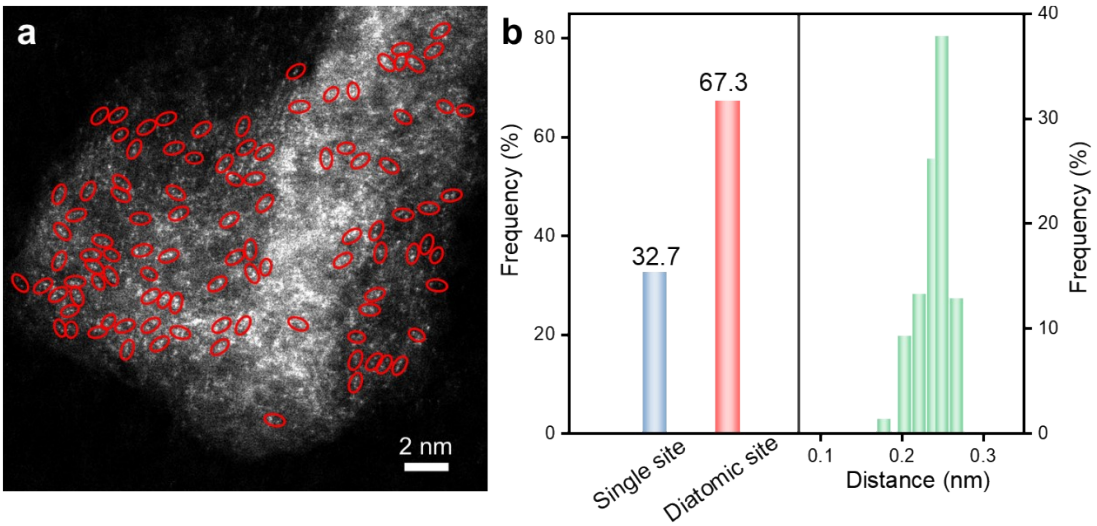

Fig. S4 (a) The AC HAADF-STEM image of L-Co_1Mn_1-NC catalyst. (b) The statistical results of atomic site density and distance distribution.

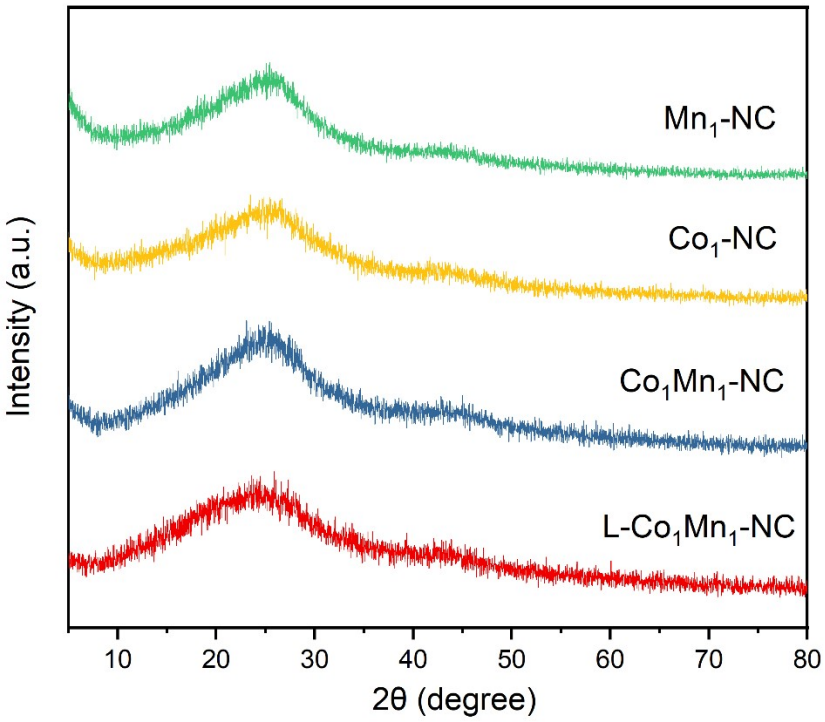

Fig. S5 The XRD patterns of L-Co_1Mn_1-NC, Co_1Mn_1-NC, Co_1-NC and Mn_1-NC.

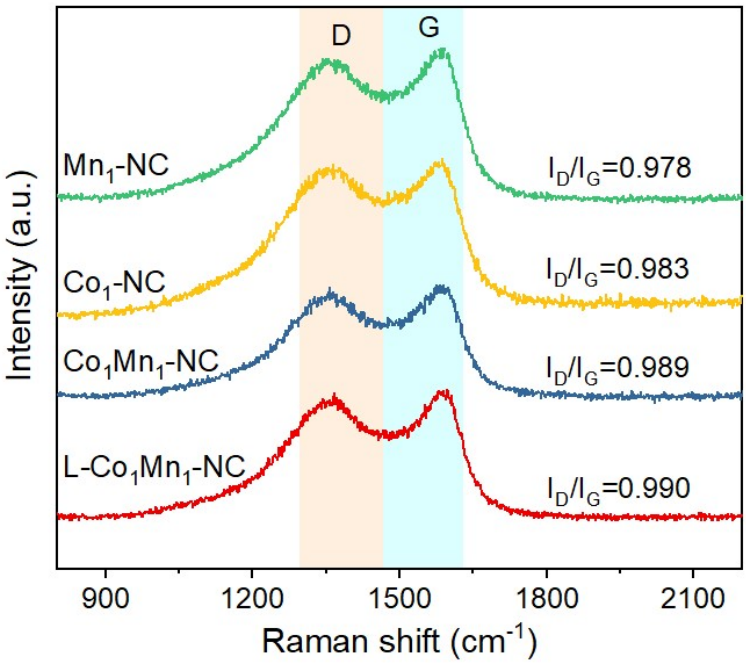

Fig. S6 The Raman spectra of L-Co_1Mn_1-NC, Co_1Mn_1-NC, Co_1-NC and Mn_1-NC.

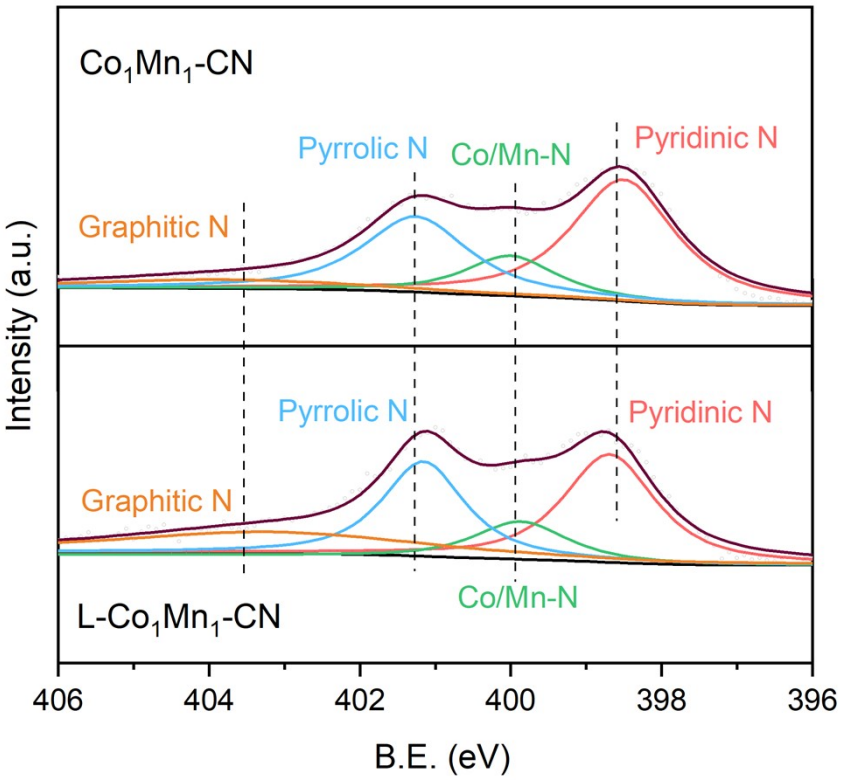

Fig. S7 N 1s XPS spectra of Co_1Mn_1-NC and L-Co_1Mn_1-NC catalysts.

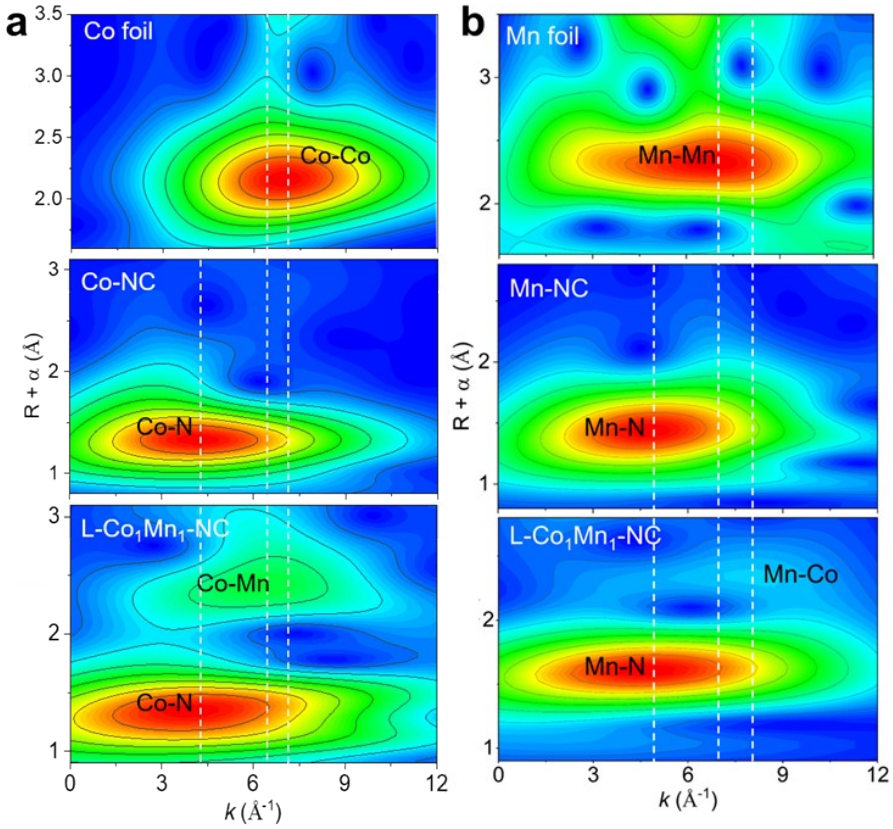

Fig. S8 WT plots for the EXAFS signals of Co K-edge (a) for Co foil, Co_1-NC, L-Co_1Mn_1-NC and Mn K-edge (b) for Mn foil, Mn_1-NC, L-Co_1Mn_1-NC.

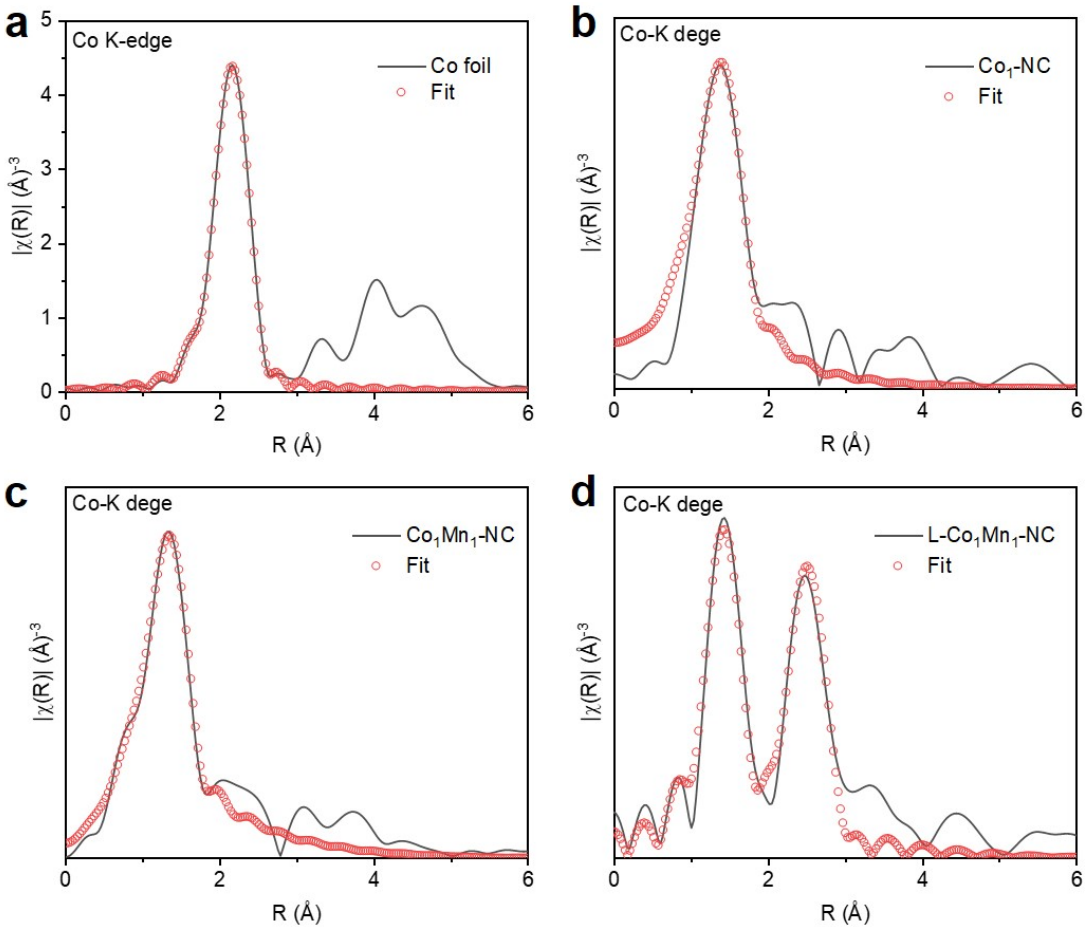

Fig. S9 The FT-EXAFS fitting spectra of (a) Co foil, (b) Co_1-NC, (c) Co_1Mn_1-NC and (d) L-Co_1Mn_1-NC catalysts at Co K-edge.

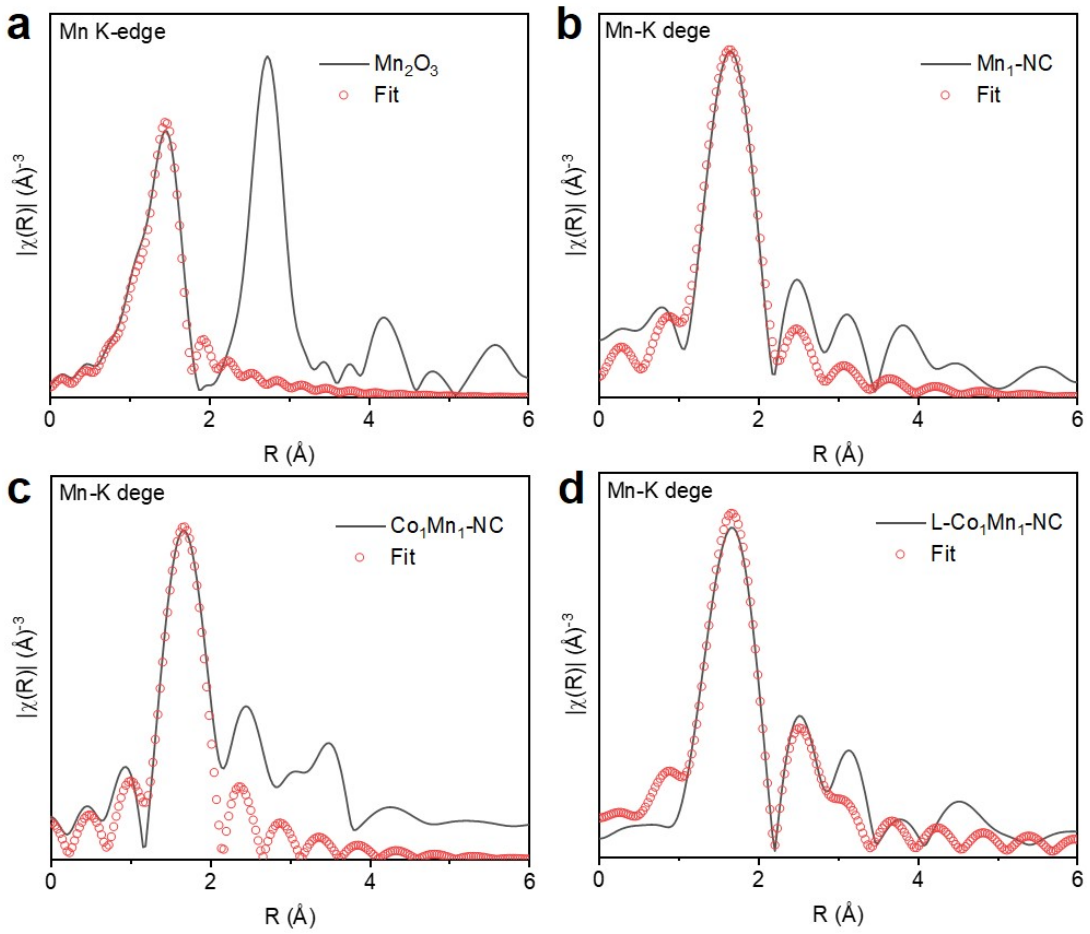

Fig. S10 The FT-EXAFS fitting spectra of (a) Mn_2O_3, (b) Mn_1-NC, (c) Co_1Mn_1-NC and (d) L-Co_1Mn_1-NC catalysts at Mn K-edge.

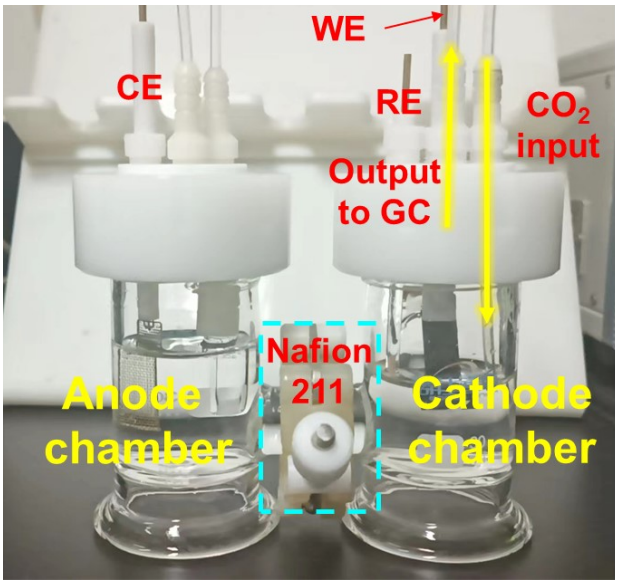

Fig. S11 Image showing the electrochemical CO_2RR measurements conducted using an H-cell setup equipped with a standard three-electrode system.

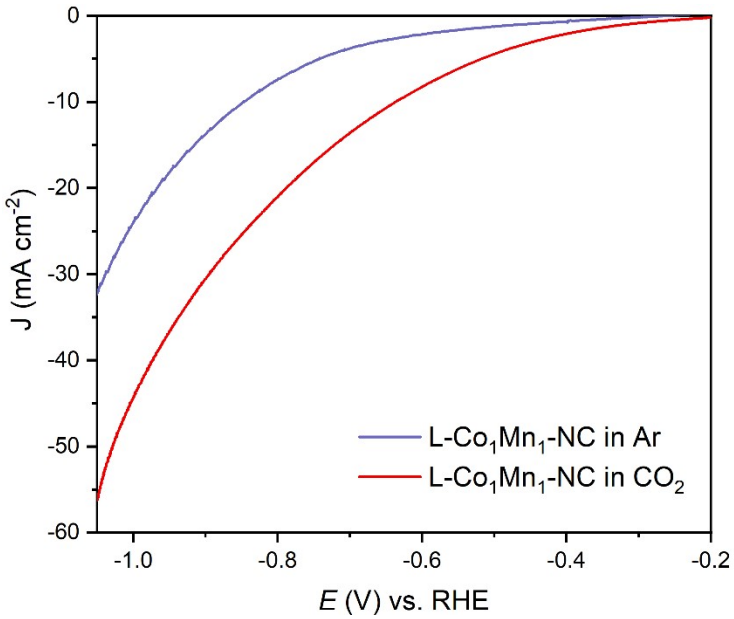

Fig. S12 The LSV comparison curves of L-Co_1Mn_1-NC catalyst in Ar- and CO_2-saturated 0.5M $KHCO_3$ solution.

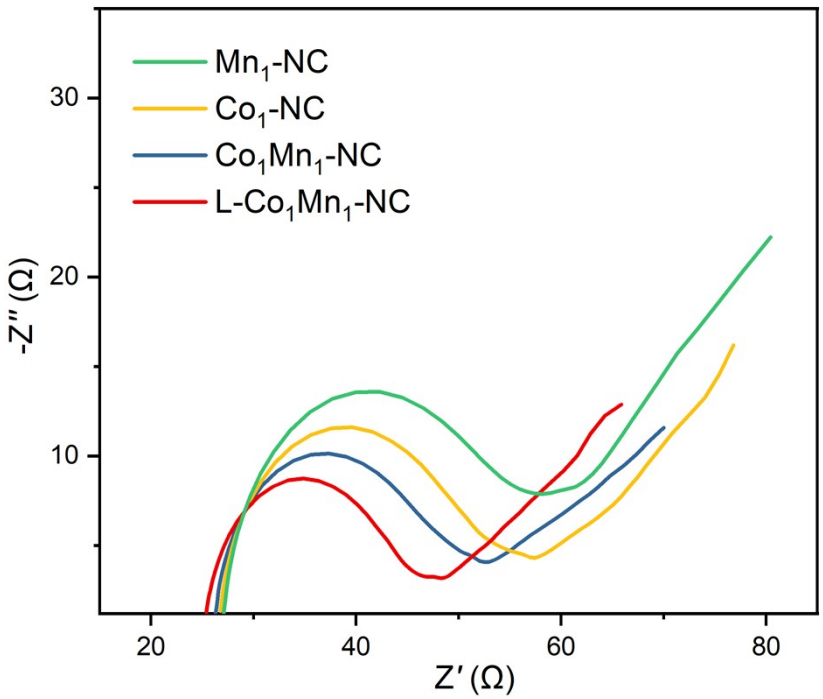

Fig. S13 The Nyquist plots of L-Co_1Mn_1-NC, Co_1Mn_1-NC, Co_1-NC, and Mn_1-NC catalyst at −0.5 V vs RHE.

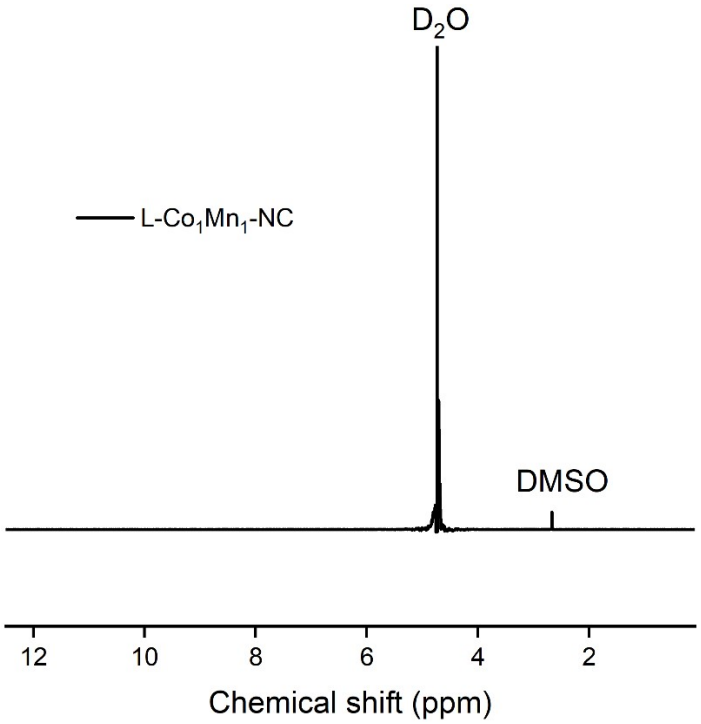

Fig. S14 The ^{1}H-NMR spectra of liquid products after CO_2RR test by L-Co_1Mn_1-NC.

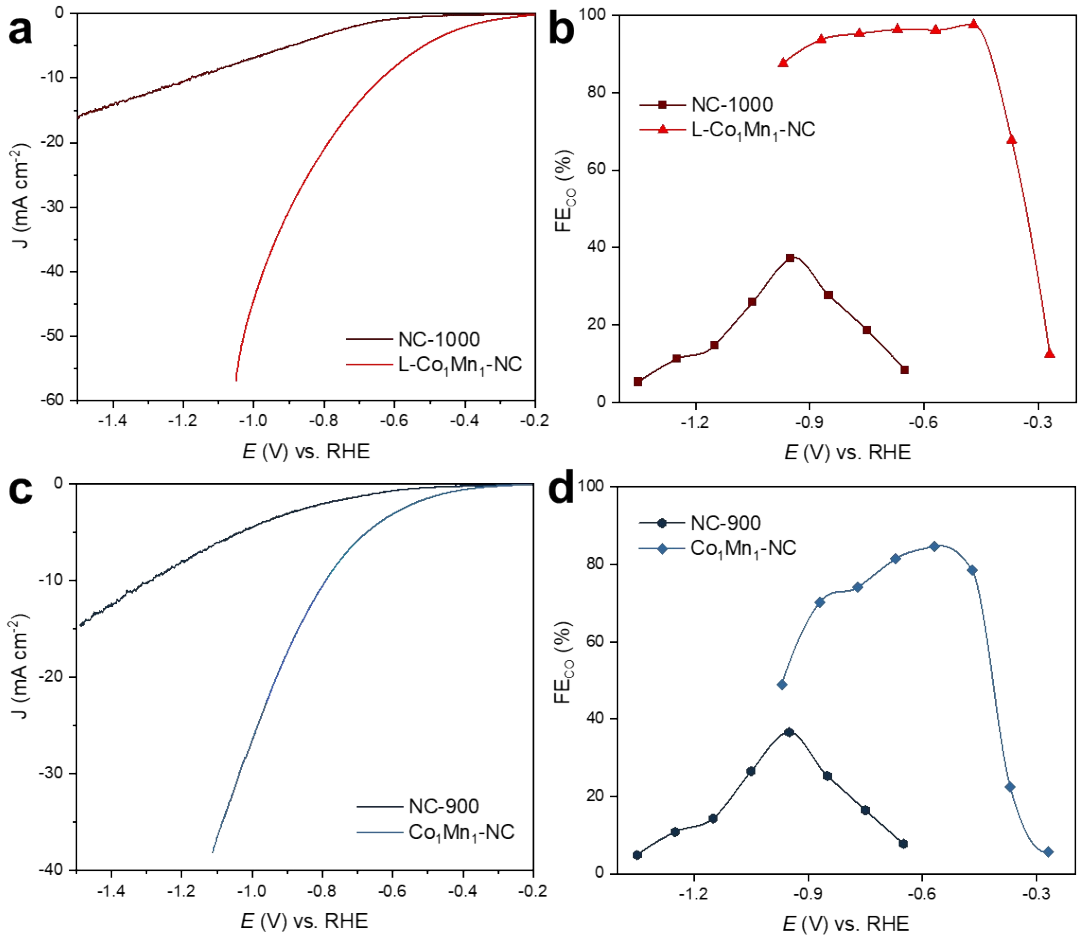

Fig. S15 The CO_2RR performances of the L-Co_1Mn_1-NC and Co_1Mn_1-NC catalysts and their carbon substrate counterparts. (a, c) Polarization curves. (b, d) FE_{CO}.

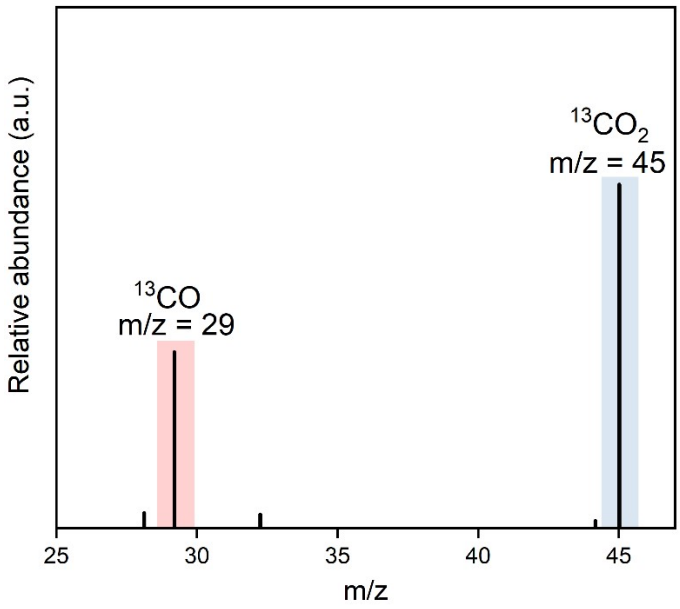

Fig. S16 Mass spectrometry signal of CO_2RR by using $^{13}CO_2$ as the electrocatalytic feedstock.

The study distinctly identified the peaks at positions 29 and 45 as corresponding to the ^{13}CO product and $^{13}CO_2$ feedstock, respectively. It is noteworthy that there was evidence of slight air leakage in the system, as evidenced by the detection of nitrogen (N_2 at 28) and oxygen (O_2 at 32) within the system.

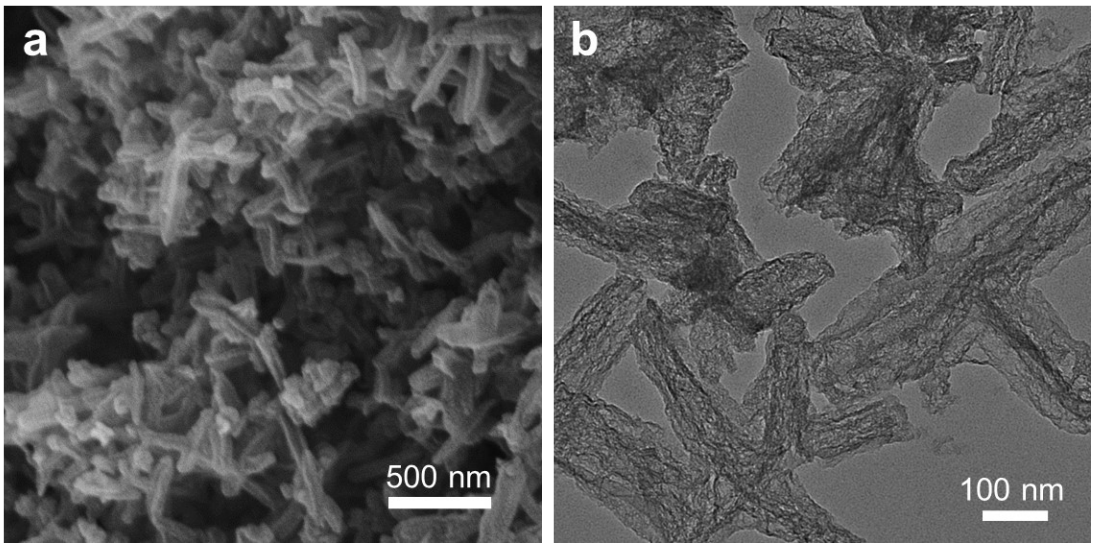

Fig. S17 The SEM (a) and TEM (b) images of L-Co_1Mn_1-NC catalyst after CO_2RR stability test.

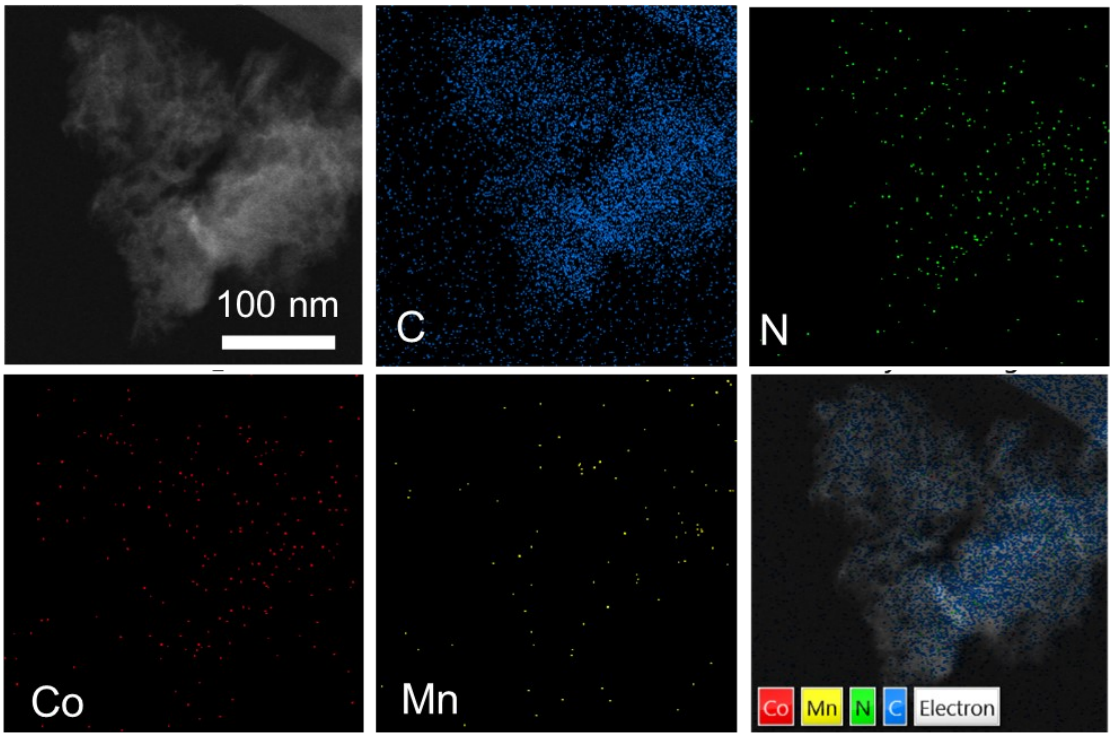

Fig. S18 EDS mappings of L-Co_1Mn_1-NC catalyst after CO_2RR, suggesting that Co, Mn, C, and N were still uniformly distributed on the carbon support.

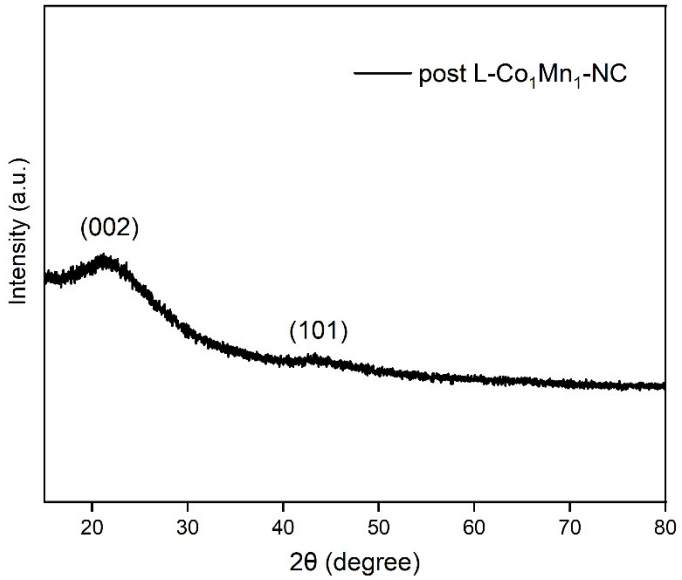

Fig. S19 The XRD pattern of L-Co_1Mn_1-NC catalyst after CO_2RR stability test.

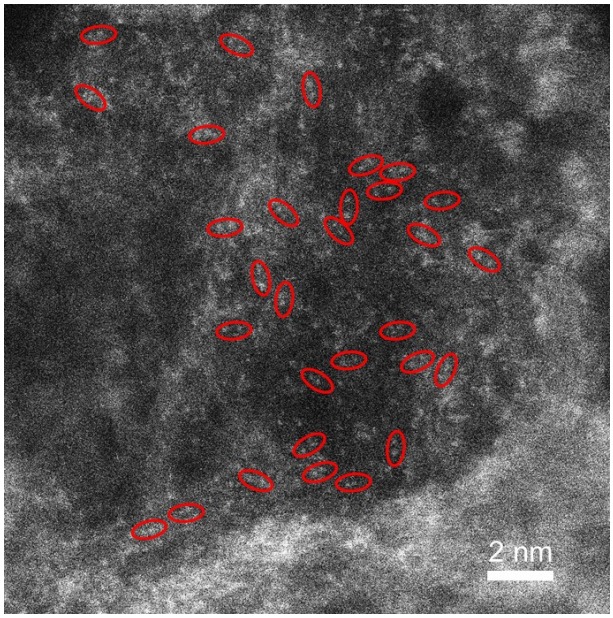

Fig. S20 The AC HAADF-STEM image of L-Co_1Mn_1-NC catalyst after CO_2RR.

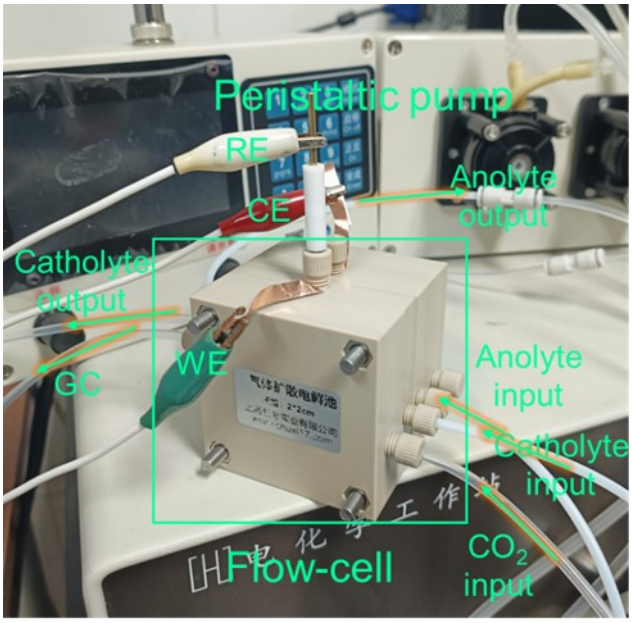

Fig. S21 The structure photograph of the home-made CO_2RR flow cell.

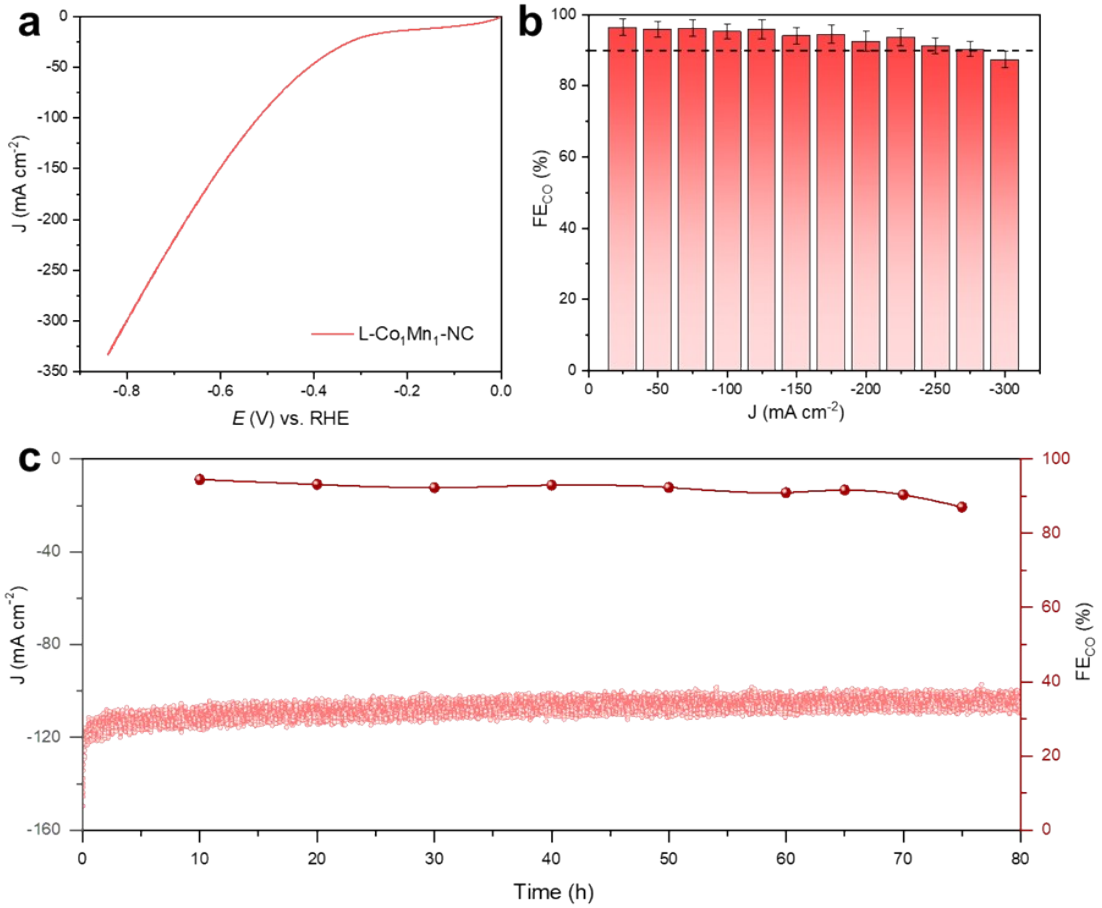

Fig. S22 CO_2RR performance of L-Co_1Mn_1-NC catalyst employing flow cell. (a) polarization curve. (b) FE_{CO}. (c) Chronoamperometry at –0.55 V for 50 h. The FE_{CO} was tested ever 10 h of electrolysis.

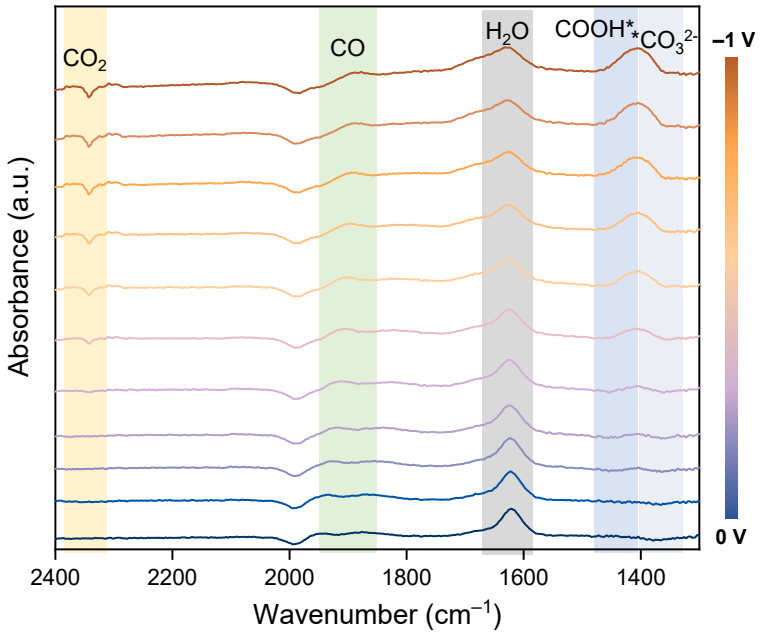

Fig. S23 The in situ ATR-SEIRAS spectra of L-Co_1Mn_1-NC catalyst.

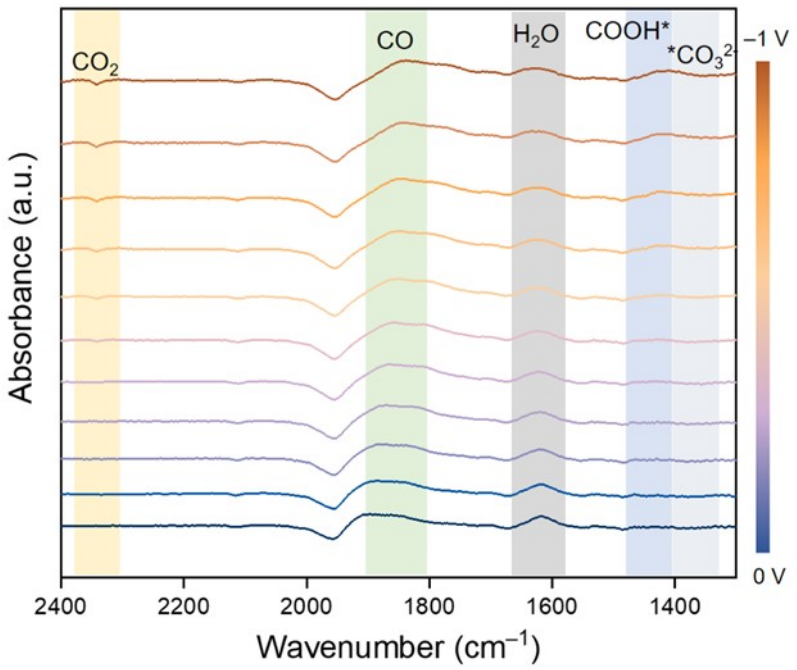

Fig. S24 The in situ ATR-SEIRAS spectra of Co_1Mn_1-NC catalyst.

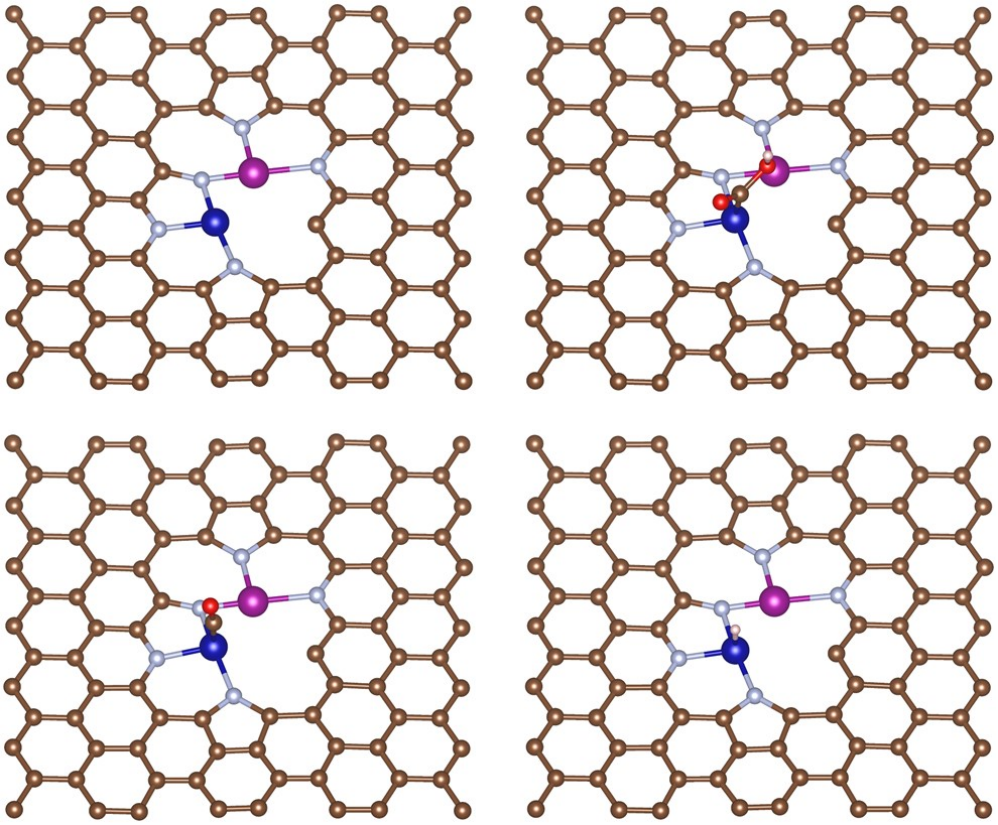

Fig. S25 Optimized atomic structures of L-Co_1Mn_1-NC with COOH*, CO* and intermediates adsorbed on Co site.

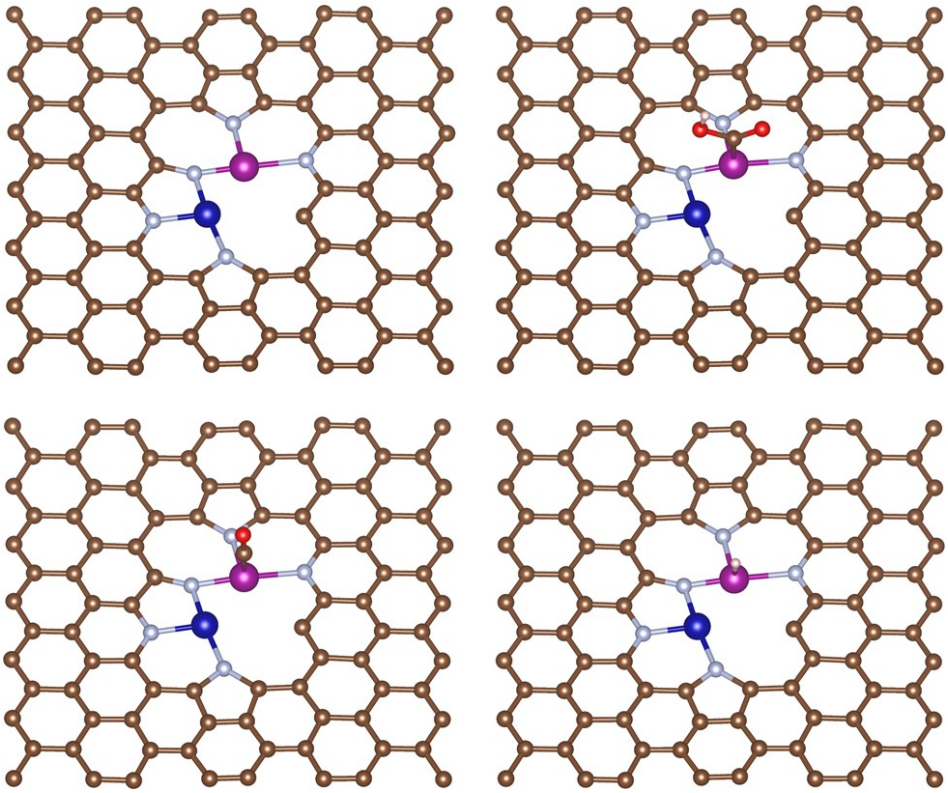

Fig. S26 Optimized atomic structures of L-Co_1Mn_1-NC with COOH*, CO* and intermediates adsorbed on Mn site.

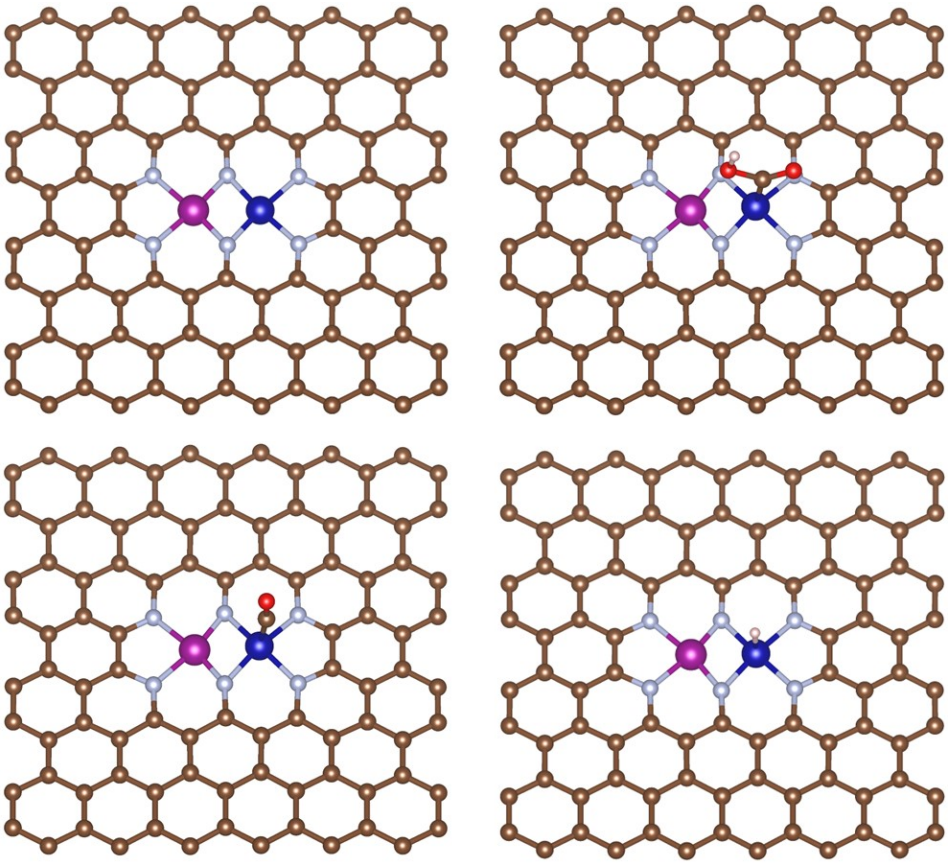

Fig. S27 Optimized atomic structures of Co_1Mn_1-NC with COOH*, CO* and intermediates adsorbed on Co site.

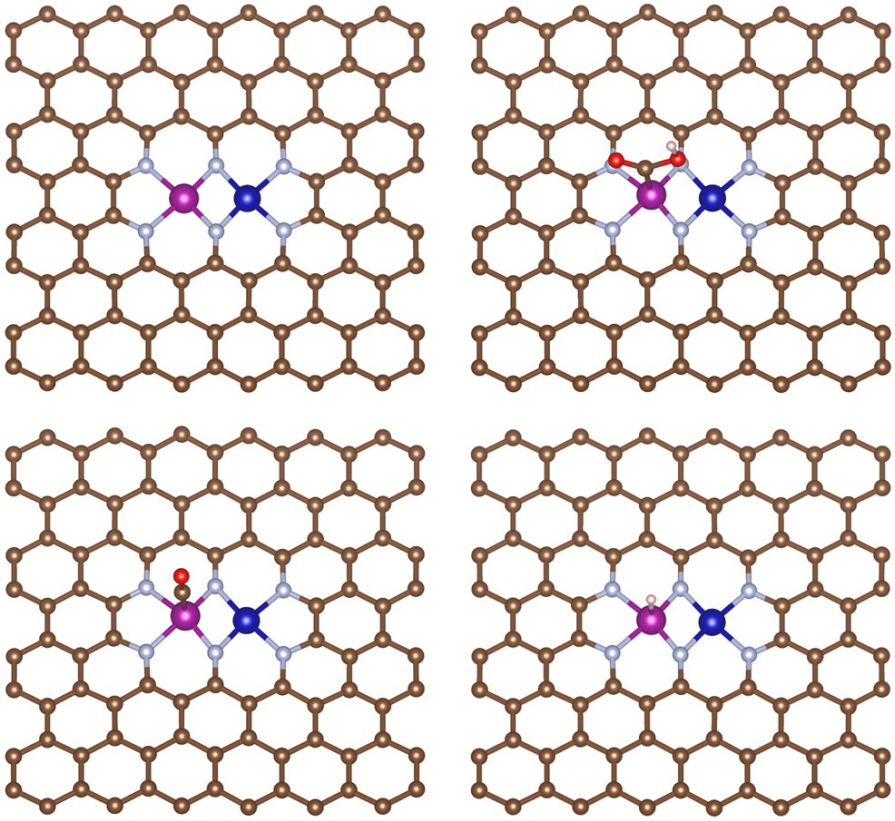

Fig. S28 Optimized atomic structures of L-Co_1Mn_1-NC with COOH*, CO* and intermediates adsorbed on Co site.

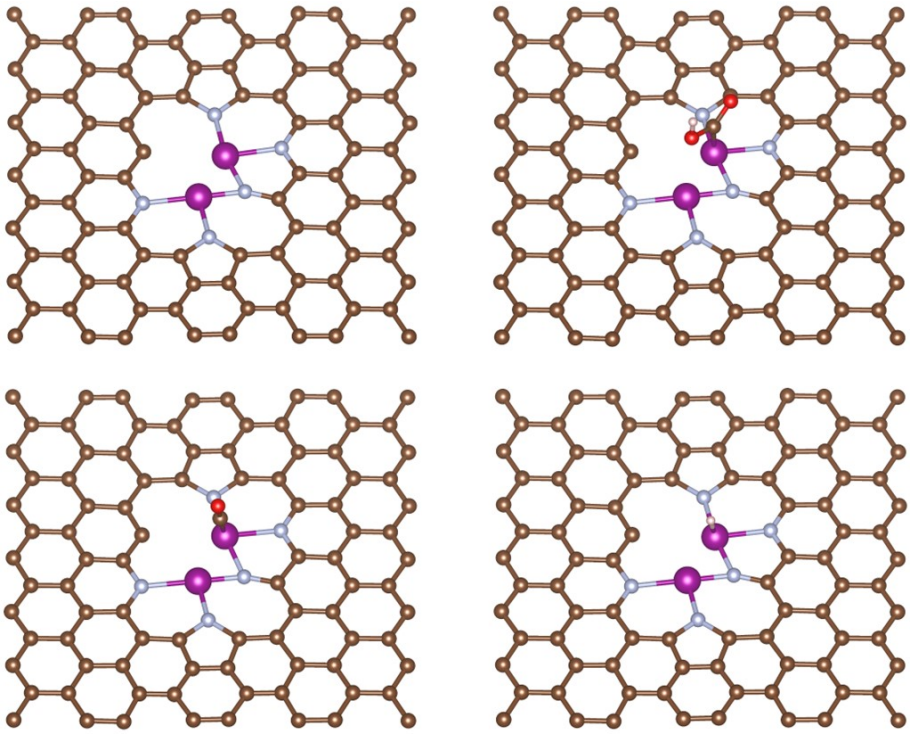

Fig. S29 Optimized atomic structures of L-Co_2-NC with COOH*, CO* and intermediates adsorbed on Co site.

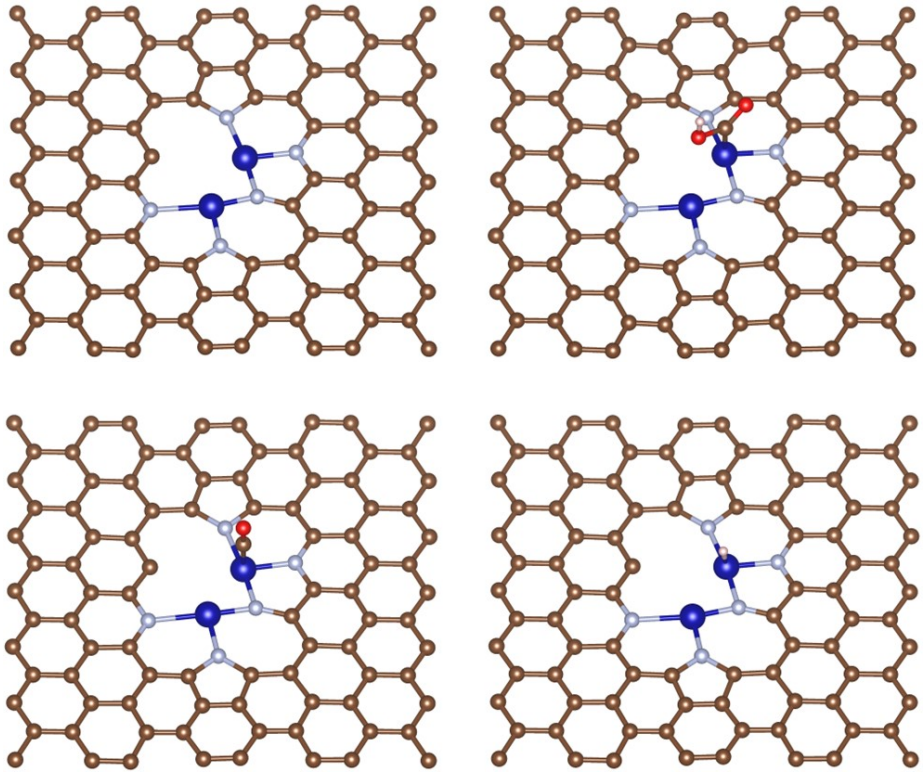

Fig. S30 Optimized atomic structures of L-Mn_2-NC with COOH*, CO* and intermediates adsorbed on Mn site.

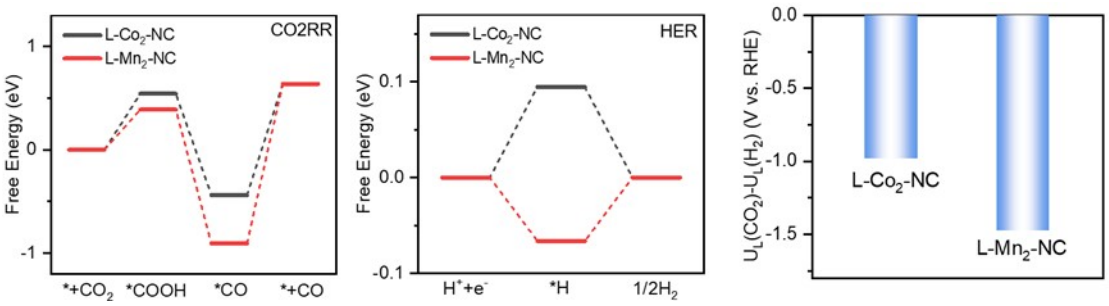

Fig. S31 The Gibbs free energy diagrams for the CO_2 to CO and HER as well as the calculated limiting potentials difference of CO_2RR and HER.

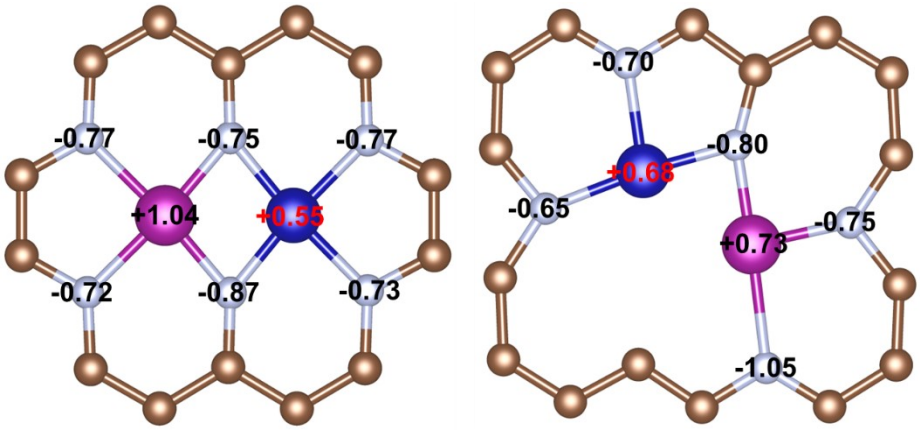

Fig. S32 Bader charge analysis of Co_1Mn_1-NC and L- Co_1Mn_1-NC catalysts.

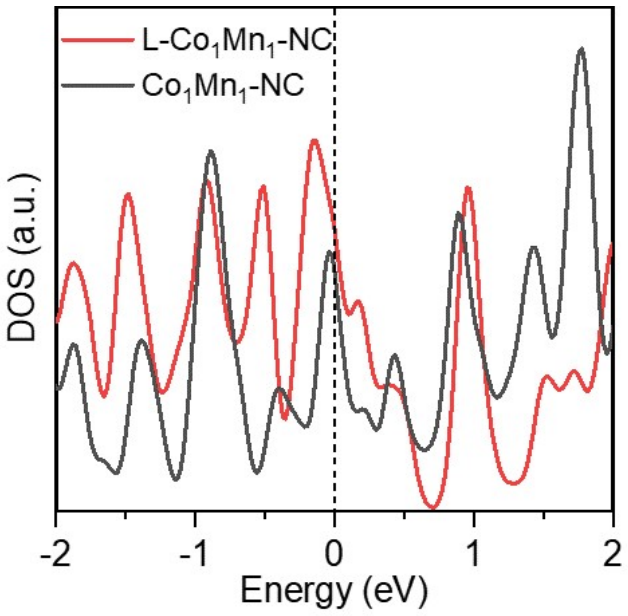

Fig. S33 Total DOS for Co_1Mn_1-NC and L- Co_1Mn_1-NC catalyst.

Table S1. ICP-OES results of the L-Co_1Mn_1-NC, Co_1Mn_1-NC, Co_1-NC, and Mn_1-NC catalysts.

Samples	Co (wt%)	Mn (wt%)
L-Co_1Mn_1-NC	0.52	0.36
Co_1Mn_1-NC	0.55	0.38
Co_1-NC	0.91	/
Mn_1-NC	/	0.88

Table S2. Structural parameters extracted from the Co K-edge EXAFS fitting (S_0^2=0.72).

Sample	Scattering pair	CN	R(Å)	$\sigma^2(10^{-3}Å^2)$	R factor
Co_1-NC	Co−N	4.2	1.94	0.006	0.009
Co_1Mn_1-NC	Co−N	3.7	1.93	0.006	0.006
L-Co_1Mn_1-NC	Co−N	3.2	1.93	0.010	0.008
	Co−Mn	0.8	2.68	0.009	
Co foil	Co−Co	12*	2.49	0.004	0.001

S_0^2 is the amplitude reduction factor; CN is the coordination number; R is interatomic distance (the bond length between Co central atoms and surrounding coordination atoms); σ^2 is Debye-Waller factor (a measure of thermal and static disorder in absorber-scatterer distances); R factor is used to value the goodness of the fitting.

* This value was fixed during EXAFS fitting, based on the known structure of Co foil.

Error bounds that characterize the structural parameters obtained by EXAFS spectroscopy were estimated as N ± 20%; R ± 1%; σ^2 ± 20%.

Table S3. Structural parameters extracted from the Mn K-edge EXAFS fitting (S_0^2=0.74).

Sample	Scattering pair	CN	R(Å)	$\sigma^2(10^{-3}Å^2)$	R factor
Mn_1-NC	Mn−N	4.1	2.02	0.004	0.013
Co_1Mn_1-NC	Mn−N	4.3	2.03	0.004	0.008
L-Co_1Mn_1-NC	Mn−N	3.1	2.01	0.008	0.017
	Mn−Co	1.2	2.70	0.012	
Mn_2O_3	Mn−O	3*	1.88	0.003	0.012

S_0^2 is the amplitude reduction factor; CN is the coordination number; R is interatomic distance (the bond length between Mn central atoms and surrounding coordination atoms); σ^2 is Debye-Waller factor (a measure of thermal and static disorder in absorber-scatterer distances); R factor is used to value the goodness of the fitting.

* This value was fixed during EXAFS fitting, based on the known structure of Mn_2O_3. Error bounds that characterize the structural parameters obtained by EXAFS spectroscopy were estimated as N ± 20%; R ± 1%; σ^2 ± 20%.

Table S4. CO_2RR Performance comparison of various reported Co-based and Mn-based catalysts under the similar conditions.

Catalysts	Overpotential	J_{CO}	FE_{CO}	TOF	Refs.
L-Co_1Mn_1-NC	360	3.5	97.6	1067	This work
	860	34.7	87.6	10535	
Co-N-Ni/NPCNSs	370	3.2	96.4	2049	4
Co-N_2	350	~6	75	5000	5
Co_1-N_4	390	~0.8	30	~80	6
CoPPc/CNT	375	~4.6	~84	~1200	7
COF-367-Co	560	3.0	91	1900	8
NapCo@SNG	625	~0.23	95	1620	9
CoN_5	620	/	99	480.2	10
MCs-(N,O)	440	13.7	94.5	/	11
MnO_2-NS/NF	310	14.1	71	/	12
Mn-N-C	490	~3.3	~65	/	13
Mn-N-C	490	~0.7	~70	46	14
Mn-C_3N_4/CNT	440	14	98.8	/	15
(Cl,N)-Mn/G	490	9.2	97	38347	16

References

1. G. Kresse and J. Furthmiiller, *Comput.Mater.Sci.*, 1996. **6**, 15-50.
2. J. P. Perdew, K. Burke and M. Ernzerhof, *Phys. Rev. Lett.*, 1996. **77**, 3865-3868.
3. P. E. Blöchl, *Phys. Rev. B*, 1994. **50**, 17953-17979.
4. J. Pei, T. Wang, R. Sui, X. Zhang, D. Zhou, F. Qin, X. Zhao, Q. Liu, W. Yan, J. Dong, L. Zheng, A. Li, J. Mao, W. Zhu, W. Chen and Z. Zhuang, *Energy Environ. Sci.*, 2021, **14**, 3019-3028.
5. X. Wang, Z. Chen, X. Zhao, T. Yao, W. Chen, R. You, C. Zhao, G. Wu, J. Wang, W. Huang, J. Yang, X. Hong, S. Wei, Y. Wu and Y. Li, *Angew. Chem. Int. Ed.*, 2018, **57**, 1944-1948.
6. Z. Geng, Y. Cao, W. Chen, X. Kong, Y. Liu, T. Yao and Y. Lin, *Appl. Catal. B*, 2019, **240**, 234-240.
7. N. Han, Y. Wang, L. Ma, J. Wen, J. Li, H. Zheng, K. Nie, X. Wang, F. Zhao, Y. Li, J. Fan, J. Zhong, T. Wu, D.J. Miller, J. Lu, S.-T. Lee and Y. Li, *Chem*, 2017, **3**, 652-664.
8. S. Lin, C.S. Diercks, Y.-B. Zhang, N. Kornienko, E.M. Nichols, Y. Zhao, A.R. Paris, D. Kim, P. Yang, O.M. Yaghi and C.J. Chang, *Science*, 2015, **349**, 1208-1213.
9. J. Wang, X. Huang, S. Xi, J.M. Lee, C. Wang, Y. Du and X. Wang, *Angew. Chem. Int. Ed.*, 2019, **58**, 13532-13539.
10. Y. Pan, R. Lin, Y. Chen, S. Liu, W. Zhu, X. Cao, W. Chen, K. Wu, W.-C. Cheong, Y. Wang, L. Zheng, J. Luo, Y. Lin, Y. Liu, C. Liu, J. Li, Q. Lu, X. Chen, D. Wang, Q. Peng, C. Chen and Y. Li, *J. Am. Chem. Soc.*, 2018, **140**, 4218-4221.
11. M. Wang, Y. Yao, Y. Tian, Y. Yuan, L. Wang, F. Yang, J. Ren, X. Hu, F. Wu, S. Zhang, J. Wu and J. Lu, *Adv. Mater.*, 2023, **35**.
12. X. Peng, Y. Chen, Y. Mi, L. Zhuo, G. Qi, J. Ren, Y. Qiu, X. Liu and J. Luo, *Inorg. Chem.* , 2019, **58**, 8910-8914.
13. A.S. Varela, N. Ranjbar Sahraie, J. Steinberg, W. Ju, H.S. Oh and P. Strasser, *Angew. Chem. Int. Ed.*, 2015, **54**, 10758-10762.
14. F. Pan, W. Deng, C. Justiniano and Y. Li, *Appl. Catal. B*, 2018, **226**, 463-472.

15. J. Feng, H. Gao, L. Zheng, Z. Chen, S. Zeng, C. Jiang, H. Dong, L. Liu, S. Zhang and X. Zhang, *Nat. Commun.*, 2020, **11**, 4341.
16. B. Zhang, J. Zhang, J. Shi, D. Tan, L. Liu, F. Zhang, C. Lu, Z. Su, X. Tan, X. Cheng, B. Han, L. Zheng and J. Zhang, *Nat. Commun.*, 2019, **10**, 2980.